International Conference on Space Optics—ICSO 2018

Chania, Greece

9–12 October 2018

Edited by Zoran Sodnik, Nikos Karafolas, and Bruno Cugny

Modelization and validation of the diffraction effects in the Microcarb instrument for accurately computing the instrumental spectral response function

M. Castelnau

E. Cansot

C. Buil

V. Pascal

et al.

International Conference on Space Optics — ICSO 2018, edited by Zoran Sodnik, Nikos Karafolas, Bruno Cugny, Proc. of SPIE Vol. 11180, 111802S · © 2018 ESA and CNES · CCC code: 0277-786X/18/$18 · doi: 10.1117/12.2536019

Modelization and validation of the diffraction effects in the MicroCarb instrument for accurately computing the Instrumental Spectral Response Function

M. Castelnau[a], E. Cansot[a], C. Buil[a], V. Pascal[a], V. Crombez[b], S. Lopez[b], L. Georges[b], M. Dubreuil[b]
[a]Centre National d'Etudes Spatiales, 18 avenue Edouard Belin 31401 Toulouse Cedex 9, FRANCE;
[b]Airbus Defence & Space, 31 rue des Cosmonautes, 31402 Toulouse Cedex 4, FRANCE

ABSTRACT

MicroCarb is a space program which uses a passive Short Wave InfraRed (SWIR) spectrometer instrument. MicroCarb will provide measurements of the atmospheric concentration of the carbon dioxide at global level with a precision sufficient in order to permit to the scientific community to improve the model of the carbon cycle by understanding the mechanisms governing the exchanges of CO2 between the sources and the sinks.

The MicroCarb Instrument is currently under development at Airbus Defense & Space (ADS). Among the spectral requirements that it must meet, some concern the Instrumental Spectral Response Function (ISRF), which is a key quantity of spectrometers, needed for spectral instrument calibration and atmospheric inversion calculations.

During the development of the Instrument, ADS proposed a method based on several Fourier Transforms to compute the ISRF, based on the one developed by R. Berlich for the FLORIS Instrument [1], in order to have an accurate model of its spectral performances.

In this paper, we will explain the simulation method, which allows to take into account diffraction at the system entrance pupil, the spectrometer slit and the dispersion grating, and also the theoretical optical quality of the Instrument. We will describe the preliminary experiments ADS performed to validate this approach. We will then present the work done at ADS and CNES for validating and cross-checking the results of our computations, that required the use of advanced light propagation modules of CODE V.

Once validated, this tool allows to accurately compute the theoretical performances of a given working point, such as the Full-Width at Half Maximum (FWHM) of the ISRF, the resolution of the spectrometer and the likeness of the ISRF to a gaussian function. It is also a powerful tool to quickly compute many ISRFs and thus carry out trade-offs on several parameters of the instrument.

Finally, by including this static computation into a loop and by varying the radiance inside the slit, it is possible to obtain dynamic ISRFs of complex scenes on the ground, and thus have a complete and validated model of the spectral performances of the MicroCarb instrument.

Keywords: carbon dioxyde, spectrometer, echelle grating, ISRF, diffraction

1. INTRODUCTION

The COP21 climate conference has taken place in December 2015 in Paris, France. The agreement signed has enlightened the criticality of greenhouse gases in the global warming process. In this context, France has decided to kick-off the MicroCarb project that will allow for monitoring of the major greenhouse gases as CO2. The mission main objective is to monitor carbon fluxes between the atmosphere and the Earth surface. The project will provide data continuity from a European source to the worldwide climate scientific community: MicroCarb will help improving the understanding of the carbon cycle and its implication on climate change.

AIRBUS Defence and Space has been selected by the French Agency CNES for the design and development of the MicroCarb instrument, able to monitor very precisely greenhouse gases concentration (better than 1 ppm for CO2) in the atmosphere through passive sounding thanks to a very compact spectrometer, offering probationary capabilities to prepare

next generation satellites (spectral imagery capability). MicroCarb will be launched in 2021. It will follow on the American OCO2, launched in 2014, the Japanese GoSat and Gosat-2 (2009 and 2018) and the Chinese TanSat (2017) from 2021 to 2026.

The instrument must be able to operate with the required accuracy aboard Myriade satellite bus. One of the fundamental characteristics of the MicroCarb instrument is its compactness with a volume envelope near to 510 (l) x 765 (H) x 1270 (L) mm. The full preliminary design of the instrument has been detailed by F. Pasternak and al. in [2]. We will only recall here the concept of the optical design, shown in Figure 1. The whole instrumental concept of this echelle spectrometer, allowing to acquire four spectral bands on a single detector array, is under an ADS patent. The main characteristics of this instrument are summarized in Table 1.

Table 1: Main characteristics of the Instrument

Performance	**Target**			
Number of spectral bands	4			
Central wavelength of the spectral bands (nm)	764	1608	2037	1273
Observed gas	O_2	CO_2	CO_2	O_2
Spectral resolution	24 000			
On-ground total Field Of View at Nadir (across-track (ACT) km x along-track (ALT) km)	13.5 x 9			

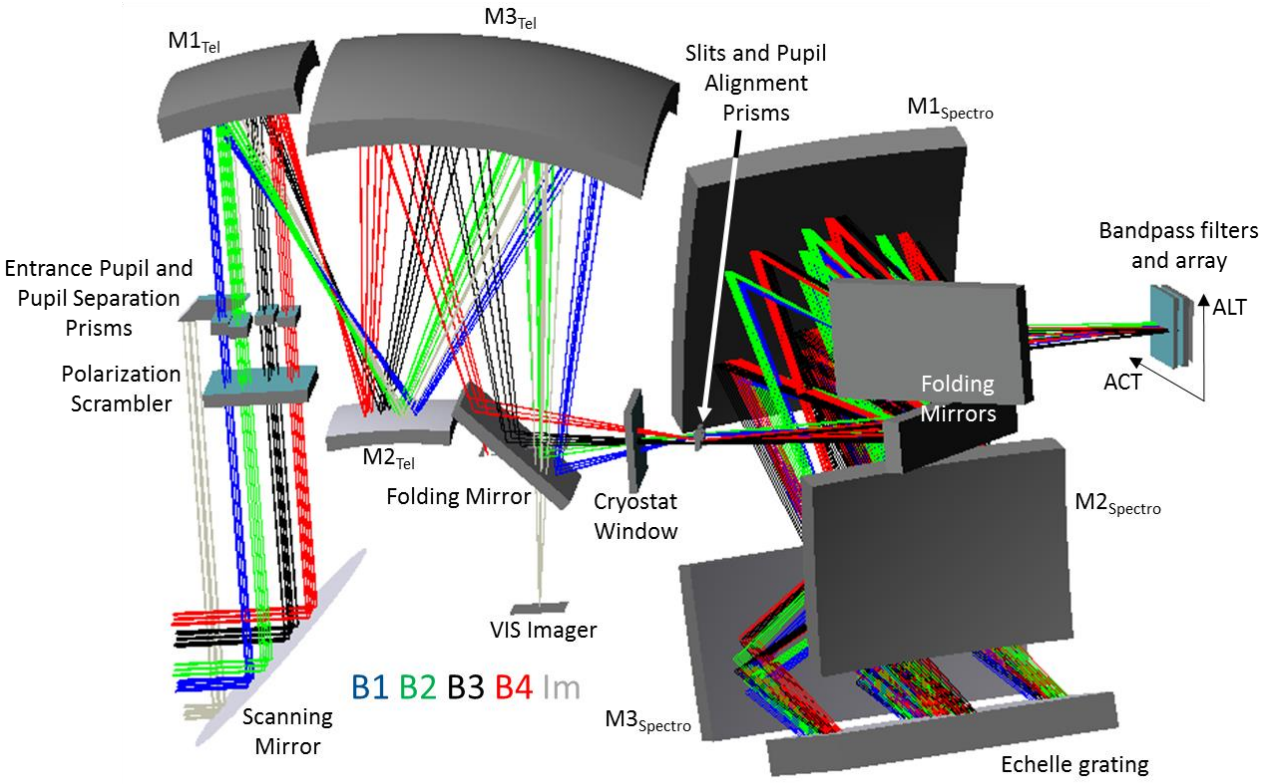

Figure 1. Optical layout of the instrument. The reference rays for the central wavelength of each spectral band are shown.

After the scanning mirror, the incoming light goes through the polarization scrambler to the Pupil Separation Prisms (PSP), whose aim is to separate the four channels at the telescope focal plane along the across-track (ACT) direction while maintaining the same scene seen on Earth by all channels: each prism is dedicated to one spectral band, its size is driven by the size of the subpupil of its spectral channel and is adequately bandpass coated. The entrance pupil mask is put into the PSP assembly and every sub-pupil is rectangular. The telescope is a Three-Mirror Anastigmat (TMA) with an intermediate image.
Then, as the four channels are spatially separated at telescope focal plane, they all have their own slit at the entrance of the spectrometer. The slits are immediately followed by the Pupil Alignment Prisms (PAP), that superimpose the image of each subpupil onto the echelle grating, which is the pupil of the spectrometer. Doing so, the sizes of the grating and of the spectrometer are limited.
The beam is diffracted at high orders by the echelle grating, and after another pass into the spectrometer TMA, the four channels are focused on a single detector array, placed just behind very narrow band-pass filters, as depicted in Figure 2. In this concept, the along-track (ALT) direction is the one of the spectral dispersion.

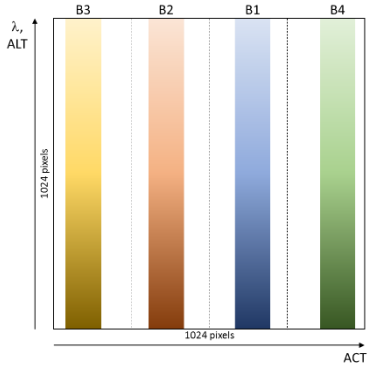

Figure 2. Distribution of spectral bands over the array

Several elements in this instrumental concept (its optical design and its accommodation, the choice of using an echelle grating, the size of the slit) have a direct impact on a key parameter of MicroCarb, namely the Instrumental Spectral Response Function (ISRF). This function represents how a pixel of the detector array, which is associated to a wavelength, reacts in relative value when the wavelength of an incoming monochromatic light on the instrument varies. As the knowledge of the ISRF associated to an instrumental concept is essential, ADS and CNES carried out important studies to develop and validate an analytical model of the ISRF.

2. MODELIZATION OF THE ISRF

The model presented by ADS for the computation of the ISRF of the MicroCarb Instrument is almost completely described in the ESA Technical Note on Floris diffraction limitations [1]. First, a simplified model of the optical system of the instrument, as shown in Figure 3, should be defined.

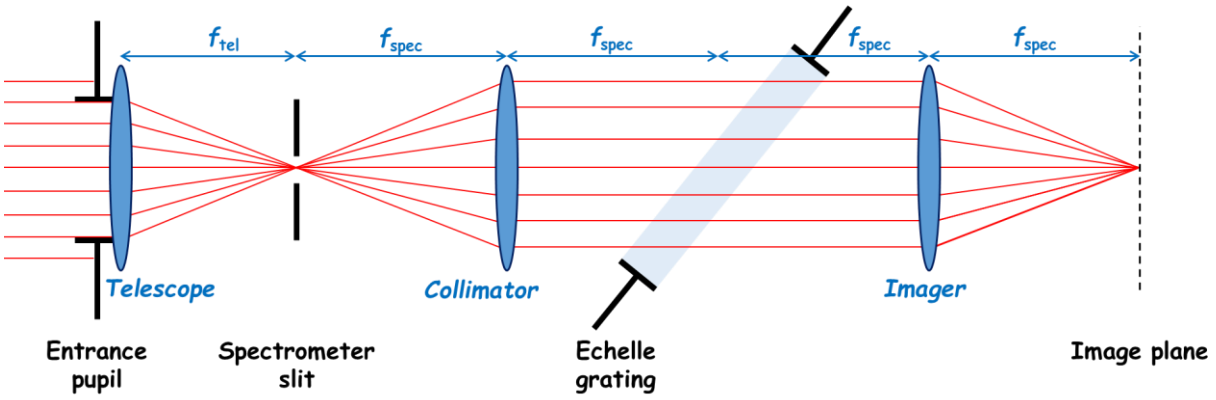

Figure 3. Simplified MicroCarb model

We consider the paraxial focal lengths of the telescope and the spectrometer, respectively f_{tel} and f_{spec}. In the case of MicroCarb, the spectrometer is used in double-pass, so the focal lengths of the imager and the collimator are the same. As in [1], we assume that the lenses are infinitely extended, that the thickness of all apertures are negligible, and that all optical components have a transmission (or reflection) factor of 1.

The computation of the ISRF is based on an analytical model of light propagation with Fourier Transforms. The incident monochromatic electromagnetic field on the instrument is represented by its wavelength λ_0 and its complex amplitude U with a phase defined by its angle of incidence α in the ALT direction and a constant amplitude U_0 on the entrance pupil. An electromagnetic field with a null phase then gives a Point Spread Function (PSF) centered on the slit of the spectrometer.

The different calculation steps are as follows. The meaning and the values of the parameters used in the equations below are defined in Table 2. Given data are typical, and are not the final one chosen for the design of the instrument.

Table 2. Instrumental parameters involved in the computations

Parameter name	**Parameter variable**	**Parameter typical value**				Unit
Spectral bands	**-**	**B1**	**B2**	**B3**	**B4**	-
Minimal Wavelength	λ_{min}	758.3	1596.8	2023.0	1264.6	nm
Average Wavelength	λ_{ave}	763.5	1607.9	2037.1	1273.4	nm
Maximal Wavelength	λ_{max}	768.8	1618.9	2051.1	1282.2	nm
Telescope						
Entrance pupil size in ACT	*dep_act*	17.10	17.10	17.10	17.10	mm
Entrance pupil size in ALT	*dep_alt*	4.85	5.50	5.79	5.00	mm
Focal length of the telescope	*f_tel*	63.1				mm
WFE of the telescope	*WFE_tel*	Extracted from the CODE V optical design				
Spectrometer						
Focal length of the spectrometer	*f_spec*	233.0				mm
Geometrical size of the entrance pupil on the grating in ALT	*dg_alt*	74				mm
WFE of the spectrometer	*WFE_spectro*	Extracted from the CODE V optical design				

We note $\prod h$ the rectangular function of width h and amplitude 1. The variable x stands for the ACT direction and y for the ALT direction.

- Definition of the incoming signal on the instrument:

$$U_{BeforePup}(\lambda_0, x_{Pup}, y_{Pup}) = U_0 . e^{\frac{2i\pi}{\lambda_0}.\tan(\alpha).y_{Pup}}. \quad (1)$$

- Signal windowing by the entrance pupil (width in ACT: dep_alt, and width in ALT: dep_alt):

$$U_{AfterPup}(\lambda_0, x_{Pup}, y_{Pup}) = U_{BeforePup}(\lambda_0, x_{Pup}, y_{Pup}) . \prod \frac{x_{Pup}}{dep\_act} . \prod \frac{y_{Pup}}{dep\_alt}. \quad (2)$$

- Addition of the wave front error (WFE) of the telescope to the phase on the extent of the pupil:

$$U_{AfterPup}(\lambda_0, x_{Pup}, y_{Pup}) = U_{AfterPup}(\lambda_0, x_{Pup}, y_{Pup}) . e^{2i\pi.WFE\_tel(x_{Pup}, y_{Pup})}. \quad (3)$$

- Propagation of the light to the slit of the spectrometer with a 2D FFT:

$$U_{BeforeSlit}(\lambda_0, x_{Slit}, y_{Slit}) = FT\left[U_{AfterPup}(\lambda_0, x_{Pup}, y_{Pup})\right]_{\left(\frac{x_{Slit}}{\lambda_0 . f\_tel}, \frac{y_{Slit}}{\lambda_0 . f\_tel}\right)}. \quad (4)$$

- Signal windowing by the slit (width in ACT: s_alt, and width in ALT: s_alt):

$$U_{AfterSlit}(\lambda_0, x_{Slit}, y_{Slit}) = U_{BeforeSlit}(\lambda_0, x_{Slit}, y_{Slit}) . \prod \frac{x_{Slit}}{s\_act} . \prod \frac{y_{Slit}}{s\_alt}. \quad (5)$$

- Propagation of the light to the grating with a 2D reverse FFT:

$$U_{BeforeGrating}(\lambda_0, x_{Gra}, y_{Gra}) = FT^{-1}\left[U_{AfterSlit}(\lambda_0, x_{slit}, y_{Slit})\right]_{\left(\frac{x_{Gra}}{\lambda_0 . f\_spectro}, \frac{y_{Gra}}{\lambda_0 . f\_spectro}\right)}. \quad (6)$$

- Signal windowing by the grating (width in ACT: dg_act, and width in ALT: dg_alt):

$$U_{AfterGrating}(\lambda_0, x_{Gra}, y_{Gra}) = U_{BeforeGrating}(\lambda_0, x_{Gra}, y_{Gra}) . \prod \frac{x_{Gra}}{dg\_act} . \prod \frac{y_{Gra}}{dg\_alt}. \quad (7)$$

- Addition of the WFE of the spectrometer to the phase of U on the extent of the pupil:

$$U_{AfterGrating}(\lambda_0, x_{Gra}, y_{Gra}) = U_{AfterGrating}(\lambda_0, x_{Gra}, y_{Gra}) . e^{2i\pi.WFE\_spectro(x_{Gra}, y_{Gra})}. \quad (8)$$

- Propagation of the light to the spectrometer focal plane with a 2D FFT:

$$U^{\alpha}{}_{FP}(\lambda_0, x_{FP}, y_{FP}) = FT\left[U_{AfterGrating}(\lambda_0, x_{Gra}, y_{Gra})\right]_{\left(\frac{x_{FP}}{\lambda_0 . f\_spectro}, \frac{y_{FP} . r}{\lambda_0 . f\_spectro}\right)}. \quad (9)$$

As the grating doesn't perfectly work in a Littrow configuration, we must take into account an anamorphosis factor r that acts especially on the spatial coordinates at the spectrometer focal plane, as we can see in Eq. (9). It is defined by the ratio of the cosine of the incidence angle on the grating over the cosine of the diffraction angle after the grating.

As far as the WFE are concerned, we extracted them from the optical design separately for the telescope and the spectrometer. One WFE per spectral band is considered for the telescope, as there are only few dispersive elements in it, and each spectral band is very narrow. For the spectrometer, we apply one WFE per wavelength because each wavelength takes a different path in the spectrometer after the grating. The WFE are projected on a Legendre polynomial base, which is orthogonal over a rectangular pupil, and thus suits well our pupil definition.

At each computation step, we can observe $U . \bar{U}$, a real magnitude homogeneous with an irradiance.

This calculation is done for a point source. The generation to any scene, and in particular, to a uniform scene in the ALT

field, is made by considering the scene as a set of point sources defined by their incidence angle on the instrument α. The summation is then performed at each step, in irradiance (incoherent light hypothesis). Especially, the irradiance at the spectrometer focal plane, after integration over the ACT direction, is the "optical part" of the ISRF:

$$ISRF_{optical}(\lambda_0, y_{FP}) = \sum_{ACT} \sum_{\alpha} |U^{\alpha}{}_{FP}(\lambda_0, x_{FP}, y_{FP})|^2. \quad (10)$$

To obtain the full ISRF, including the effect of the finite pixel size a, we perform a convolution with a function called $P(y)$, simulating the inter-pixel diffusion:

$$ISRF(\lambda_0, y_{FP}) = ISRF_{optical}(\lambda_0, y_{FP}) * P(y_{FP}), \quad (11)$$

Finally, we convert the y_{PF} coordinates into wavelengths by using the spectral dispersion formula evaluated at λ_0, giving a coefficient of proportionality $\Delta\lambda_0$ in nm/pixel:

$$\lambda = \lambda_0 + \frac{y_{PF}}{a}.\Delta\lambda_0. \quad (12)$$

Thus, this method allows us to take into account the diffraction effects that occur due to:

- the limited size of the entrance pupil: it is the conventional Fraunhofer diffraction theory,
- the edges of the slit: as the ISRF is defined for an extended source, it is important to consider the diffracted light coming from the field points close to the edges of the slit,
- the limited size of the grating: the echelle grating is here approximated by a basic rectangular aperture, as it works in quasi-Littrow configuration. For justification, see [1]. As both former diffraction effects enlarge the image of the entrance pupil on the grating, some diffraction may occur on this surface as its size is limited.

As an illustration of the diffraction effects within the instrument, we show in Figure 4 an example in one dimension of the irradiance at four different planes, for the average wavelength of B3 (2037.1 nm), for a point source (a) and a homogeneous scene (b). We choose this wavelength for illustration because it is the highest spectral band of the instrument, so it is the most impacted by all these effects. For those computations, we use the parameter values given in Table 2.

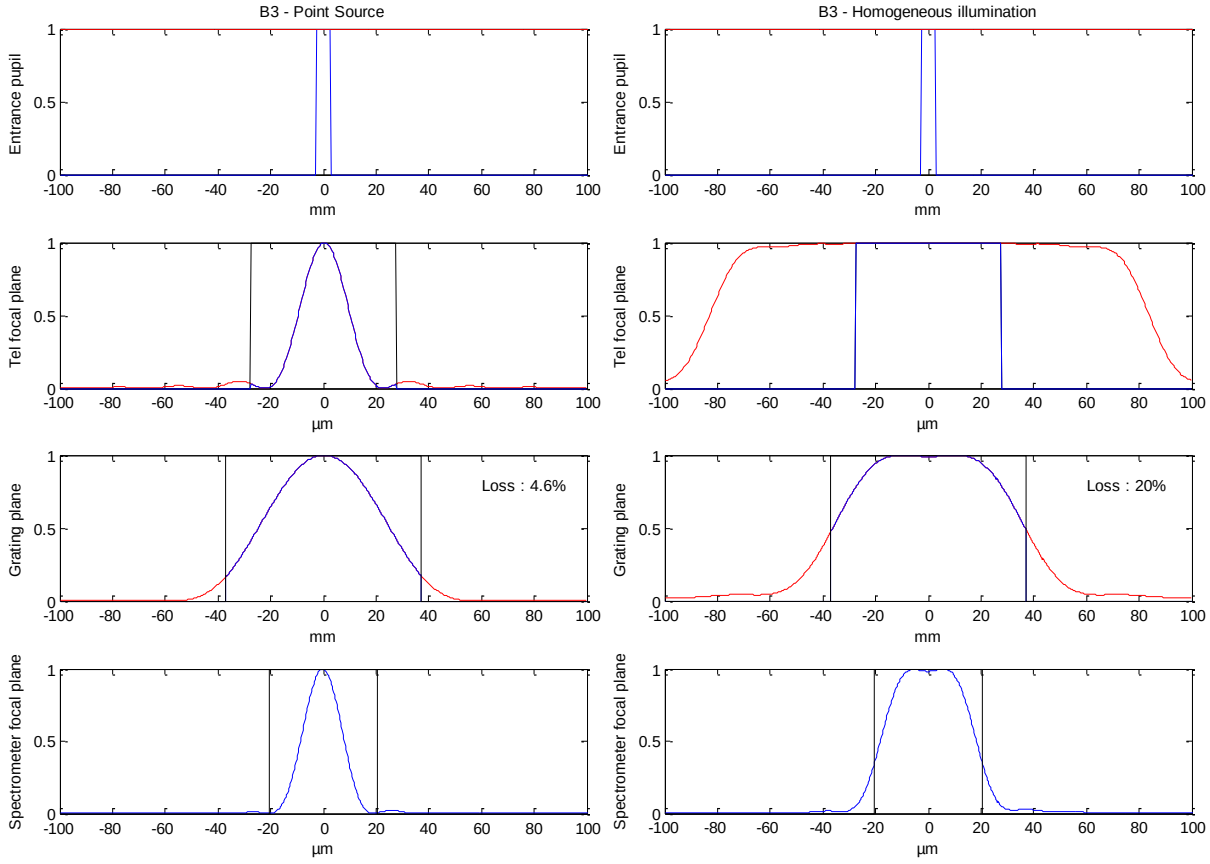

(a) (b)

Figure 4. Computed irradiance at different planes in the instrument for (a) a point source at the center of the slit, and (b) an homogeneous scene. The curves are: red - the truncated part of the signal at each plane, blue - the transmitted part of the signal, black – the slit at telescope focal plane, the size of the grating and the geometrical size of the slit on the detector at spectrometer focal plane.

We can make several observations on those figures, especially for the homogeneous source:

- The diffraction after the slit induces a significant enlargement and smooth of the projection of the rectangular entrance pupil on the grating plane with respect to the geometrical computation (graph at grating plane, case (b)). At the sight of these results, we decided to enhance the size of the grating to 100 mm in ALT, which is the maximum available size allowed by the mechanical design. It reduces the loss of signal at the grating from 20% (with the initial size of the grating) to 7.5%.
- The finite size of the grating also implies a loss in the frequency domain: this component acts as a low-pass. As a consequence, the width of the optical part of the ISRF (graph at spectrometer focal plane, case (b)) is shorter than the geometrical size of the slit on the spectrometer focal plane. Even after the convolution by the pixel function, the width remains shorter than what was computed with simple convolutions so far. Thus, as we require the sampling factor of the ISRF to be greater than 2.6, we decided to enlarge the size of the slit in the spectral dimension. A nice consequence of this increase is the fall of loss signal at the grating to 5.8%, only due to diffraction effects.

We took those decisions after several validation steps lead at CNES and ADS and described in the next section.

3. VALIDATIONS OF THE MODEL

3.1 Experimental tests at ADS

ADS developed an optical test bench in order to validate the manufacturing and alignment tolerances of the PSP and PAP assemblies. This bench owns the same optical planes as the real instrument, and is thus a good candidate to perform comparisons between real and simulated images.

We first compare the irradiance at pupil plane for a point source, as shown in Figure 5.

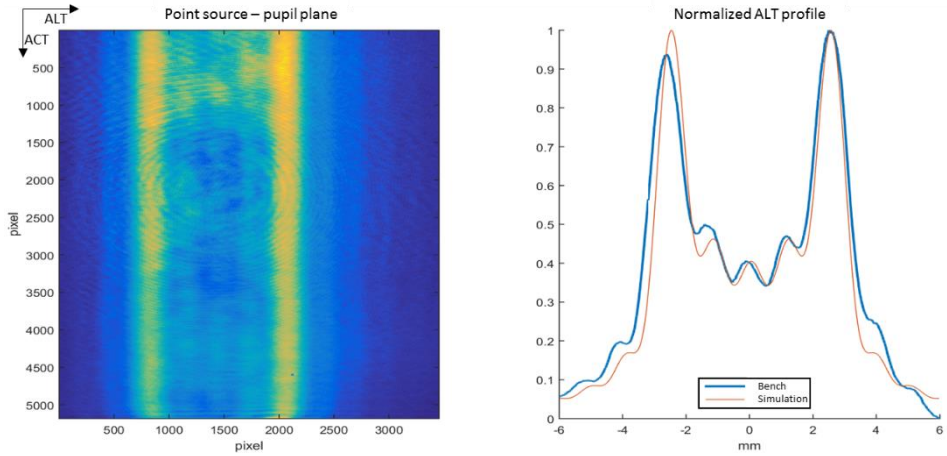

Figure 5. Left - recorded image on the bench, right - normalized ALT profiles, for a point source

The experimental ALT profile is obtained after summation of all the lines of the left image to minimize the noise. It has been seen in simulation that the profile is particularly sensitive to the position of the source in the field. Nevertheless, the model shows a good likeness to the experimental curve.

Then, we compare the irradiance at pupil plane for an extended source, as shown in Figure 6.

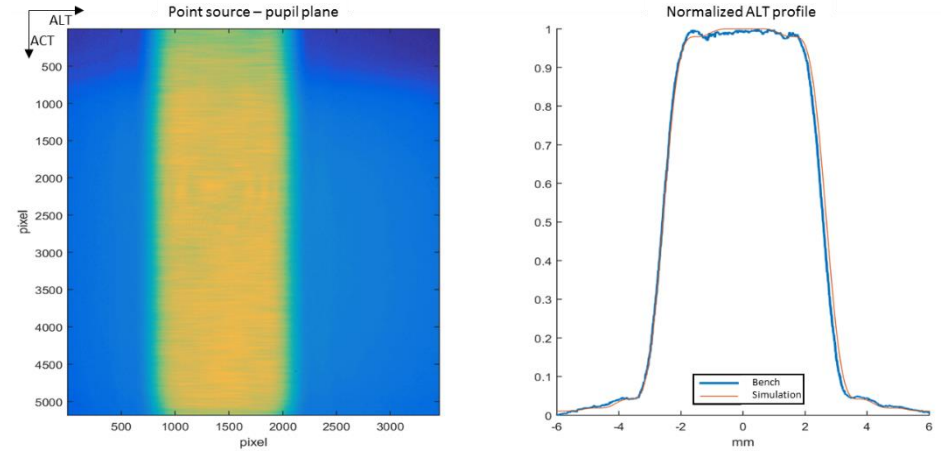

Figure 6. Left - recorded image on the bench, right - normalized ALT profiles, for an extended source

The appearance of both curves shows a particularly good similarity. The profile isn't perfectly rectangular, and the spreading of the energy far from the center is well predicted.

We also compare the diffraction pattern at the image plane for a point source, see Figure 7. We place a circular stop with a tunable diameter in the pupil plane to observe different diffraction effects. The experimental image is saturated in order to make the diffraction rings visible, and the level of the simulated image is adapted to be close to the recorded one.

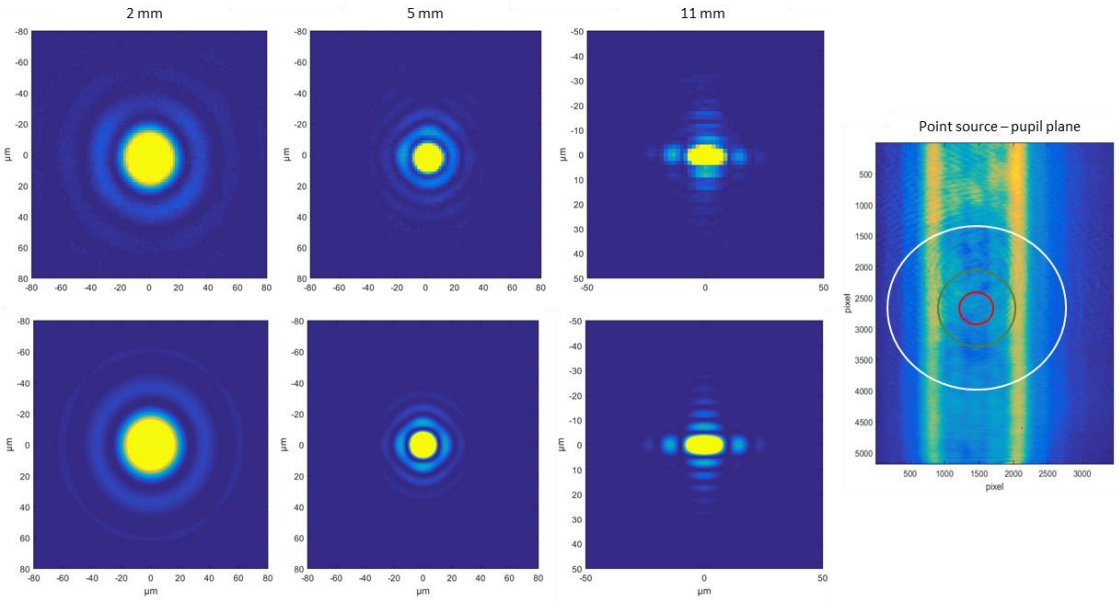

(a) (b)

Figure 7. (a): Real (top) and simulated (bottom) diffraction patterns at image plane for three different pupil size: 2 mm (left), 5 mm (middle) and 11 mm (right). (b): Representation of the size of the stop at pupil plane wrt the irradiance pattern: red circle = 2 mm, green circle = 5 mm and white circle = 11 mm.

With a stop size of 2 mm, which is smaller than the width of the enlightened area in the pupil plane, we simply see the symmetric Airy pattern linked to the size of the stop.
With a stop size of 5 mm, which is still smaller than the width of the enlightened area in the pupil plane, but is close to the edges, we begin to see an asymmetrical spot.
With a stop size of 11 mm, the pattern isn't symmetric anymore:

- in the ALT direction, we see the diffraction of the slit because the stop size is greater than the enlightened area in the pupil plane,
- in the ACT direction, we keep seeing the diffraction of the stop.

In all those cases, the simulation is very close to the experimental results.

To conclude, at pupil plane, the experimental and simulated irradiance profiles are very close for a point source and an extended scene. At focal plane, as images are saturated, we can't do quantitative comparisons, but theory and experiment give extremely similar results.

3.2 Numerical approach with CODE V

We also decided to use the BSP module of CODE V to retrieve the curves presented by ADS. This module allows the user to correctly take into account the diffraction effects that occur between the entrance and the exit pupils. To do so, the incident light beam is sampled into constant phase beamlets, that are propagated through the optical design. More details are available in the CODE V Reference Manual [3].

We use the parameters values listed in Table 2, except for the grating dimensions: we consider 100 mm in ALT for the optical useful area. Furthermore, we only compute the optical part of the ISRF for the minimum wavelength of each spectral band.
We use the spectrometer design alone for three reasons:

- the telescope is diffraction-limited over the field of the slit,

- we are able to model the direction and the curvature of the exit wavefront of the telescope in the input parameters of BSP, for each field,
- the speed gain is high.

We sample the slit into 51 points, which roughly corresponds to a point every micron. For each point, we run the pre-analysis function of BSP, in order to define:

- the number of beamlets to propagate,
- the surfaces where the aberrations are too high and force a re-sampling of the beamlets, and the associate re-sampling parameters,
- the surfaces where the beamlets meet a sharp edge, in order to re-sample them carefully.

Then we run the full propagation computation for each field, and save the irradiance we get at the spectrometer focal plane.

We also compute the propagation for 20 points out of the slit (10 on each side) separated by 1 µm, to get the contribution of their PSF that go through the slit, to the optical ISRF. For that, as CODE V doesn't propagate a beamlet if the Chief Ray is stopped by a surface, it is necessary to first propagate the beamlets to the slit surface, then save the beamlet footprint at this surface, and finally begin a new propagation until the focal plane with this footprint as an input.

We first perform a comparison between the analytical and the numerical methods for a point source. We can see on Figure 8 that the complex distribution of the PSF is remarkably well simulated by the analytical model. We also note that the irradiance given by CODE V is less resolved than the analytical model when we go far from the center of the PSF. It is a limitation caused by the trade-off between the computation speed and the precision over a large area.
We precise here that the WFE of the spectrometer are extracted over a stop size defined by the grating, and not by the image of the telescope entrance pupil, as we can see in Figure 4 that the grating is the real stop of the spectrometer.

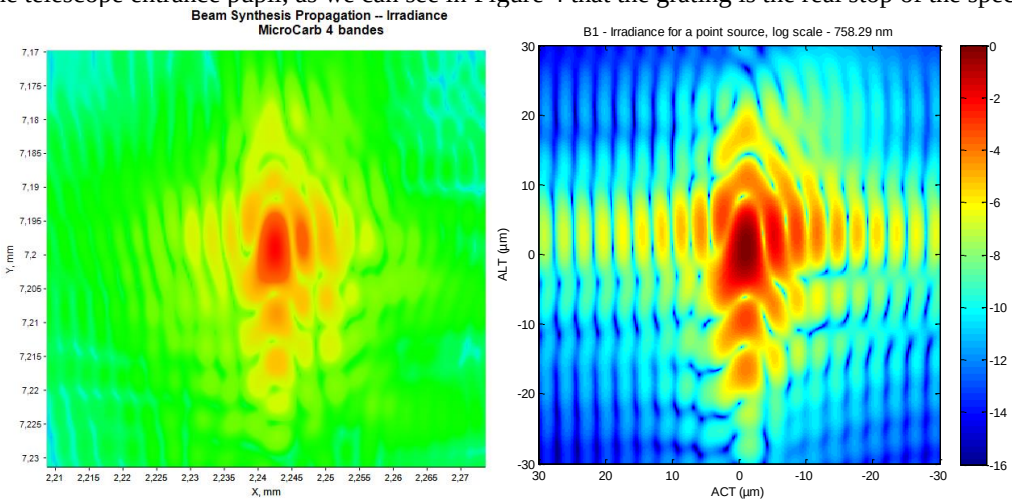

(a) (b)

Figure 8. Simulated irradiances at spectrometer focal plane with (a) the numerical model and (b) the analytical model for a point source, at 758.3 nm

We can now perform the comparison between both models with the full field of the slit uniformly illuminated. We obtain the irradiances shown in Figure 9.

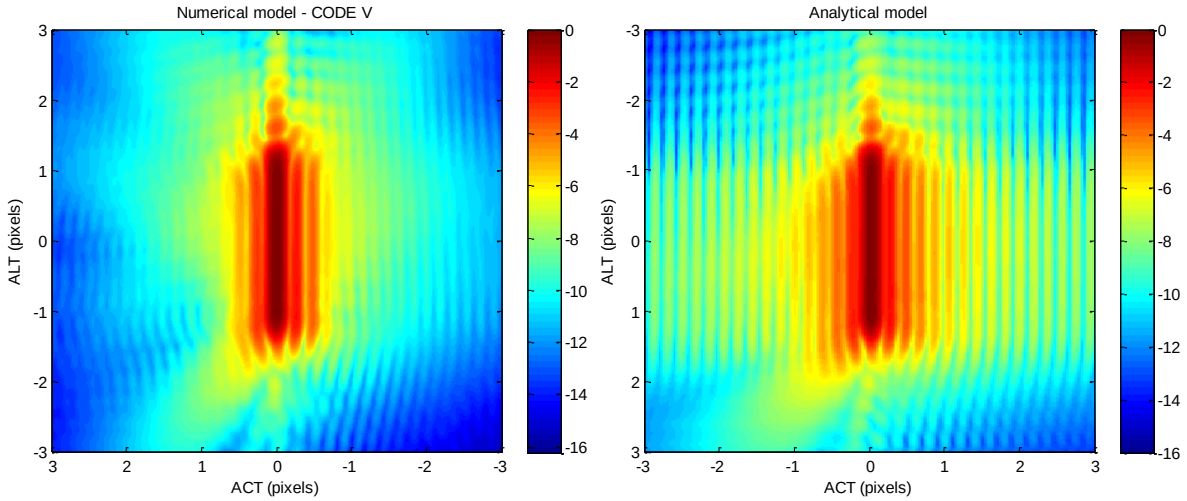

Figure 9. Simulated irradiances at spectrometer focal plane with (a) the numerical model and (b) the analytical model for the full slit, at 758.3 nm

The conclusions are quite the same as for the point source. However, we will also take the average of these images along the ACT direction, in order to compare optical ISRFs given by both methods. We finally convolve these curves by the pixel function to obtain full static ISRF. The curves for the 4 spectral bands are normalized by their area and shown in Figure 10.

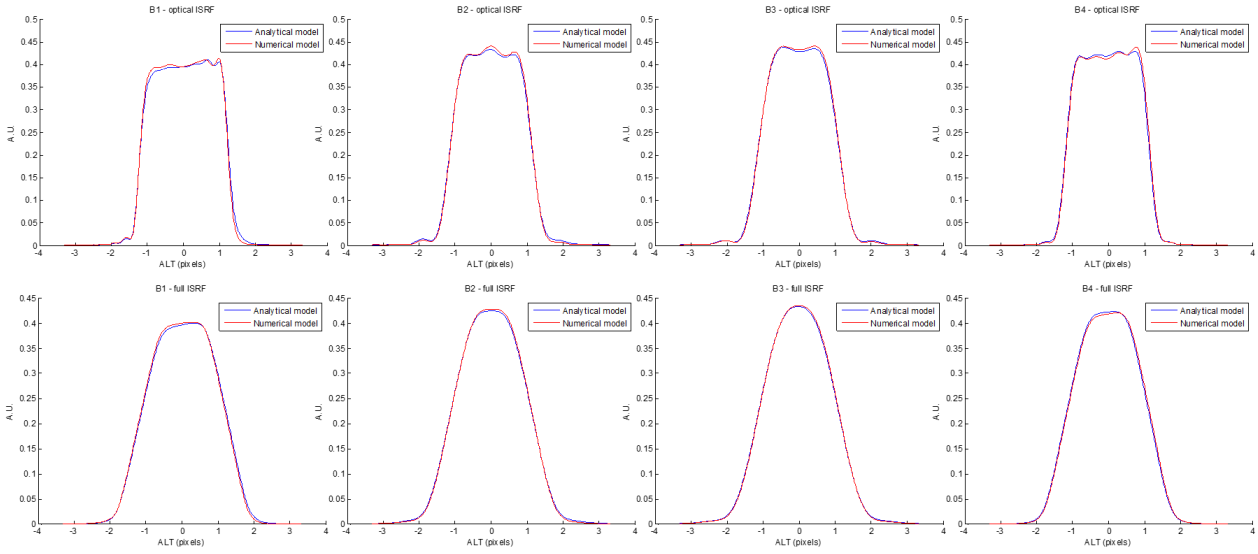

Figure 10. Optical part (top) and full (bottom) ISRF for the 4 channels of MicroCarb: left - B1, middle left - B2, middle right - B3 and right - B4, at the minimum wavelength of each spectral band

We observe a particularly good agreement between both methods, given the complexity of the computations made. We quantify the differences in Table 3 by calculating four parameters:

- The Full-Width at Half Maximum (FWHM) of the ISRF, in pixels,
- The resolution R of the instrument, given by the ratio of the wavelength in nm over the FWHM also expressed in nm,
- The likeness of the ISRF to a gaussian function, called ξ, which is the absolute value of the difference between the normalized (by its area) ISRF, and the gaussian function which has a minimum square deviation with this ISRF. We express it in percent.

- The absolute value of the difference between both full ISRF, called ε, expressed in percent.

Table 3. Summary of the performances differences between both models

B1					
	FWHM – Optical (pixels)	**FWHM – Full (pixels)**	**R**	**ξ (%)**	**ε (%)**
Numerical model	2,45	2,49	27600	13,3	1,1
Analytical model	2,47	2,50	27500	13,0	
Difference	0,6%	0,5%	0,5%	2,4%	
B2					
	FWHM – Optical (pixels)	**FWHM – Full (pixels)**	**R**	**ξ (%)**	**ε (%)**
Numerical model	2,27	2,31	29800	9,4	1,3
Analytical model	2,28	2,32	29700	8,8	
Difference	0,3%	0,3%	0,3%	6,1%	
B3					
	FWHM – Optical (pixels)	**FWHM – Full (pixels)**	**R**	**ξ (%)**	**ε (%)**
Numerical model	2,23	2,26	30500	7,9	0,8
Analytical model	2,23	2,26	30500	7,5	
Difference	0,0%	0,2%	0,2%	4,2%	
B4					
	FWHM – Optical (pixels)	**FWHM – Full (pixels)**	**R**	**ξ (%)**	**ε (%)**
Numerical model	2,33	2,37	28800	12,0	0,7
Analytical model	2,32	2,35	29000	11,5	
Difference	0,1%	0,7%	0,7%	4,0%	

Those results make us very confident in the analytical model, which gives remarkable close curves and performances to those obtained numerically, but several hundred times faster.

4. SENSITIVITY TO NON-UNIFORM SCENES IN ALT

So far, the illumination of the slit was done uniformly, and we didn't take into account the scrolling of the satellite. But we want to be able to model the ISRF of any scene during the integration time needed for covering the 9 km on-ground field of view (FOV) in ALT.

The first step is to implement the non-uniformity of the input radiance into the algorithm. We do so by replacing the constant amplitude U_0 by an on-ground spatially varying amplitude $U_0(\alpha), \alpha$ being the field angle on the telescope. Then, we can add a loop over the full FOV, and compute at each step the ISRF of the imaged non-uniform scene on the slit. We show on Figure 11 several static and dynamic ISRF at the average wavelength of B1 for uniform and non-uniform radiances on the slit. These curves are test patterns.

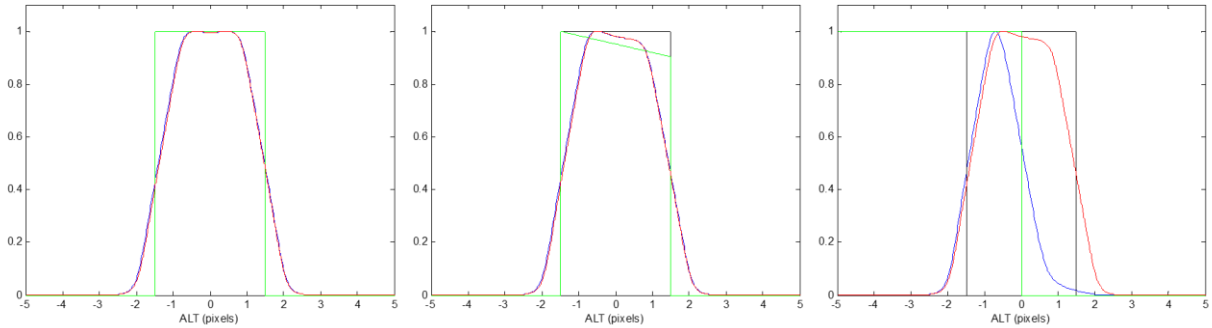

(a) (b) (c)

Figure 11. Black: geometrical size of the slit on the spectrometer focal plane, green: instantaneous radiance on the slit at the center of the FOV, blue: instantaneous ISRF and red: dynamic ISRF, obtained after integration over the full FOV. These curves are shown for 3 different scenes: (a) uniform, (b) a ramp and (c) a knife-edge function (KEF) at the center of the FOV.

We can see here that the non-uniformity of the scene may deform the ISRF. However, the instrument is a sounder, and not an imager. As a consequence, there is a scrolling of the image of the slit, and so the issues related to the non-uniformity of the scenes in ALT are reduced. Nevertheless, in order to deal with the low amount of problematic scenes regarding the shape of the ISRF, we tried to see if we could increase the robustness of the instrument to non-uniform scenes in ALT by improving the ISRF likeness to a Gaussian function. It means that we want to reduce the contribution of the geometrical shape of the slit into the shape of the ISRF. We evaluated the possibility to defocus the spectrometer in order to smooth the ISRF and bring it closer to a Gaussian function.
To do that, we extracted from CODE V the WFE for two defocused planes, and computed the coefficients of sensitivity of the Legendre coefficients to a defocus. Then the sensitivity to a defocus of the FWHM, the resolution and the likeness to a gaussian function can be evaluated. The results are plotted in Figure 12.

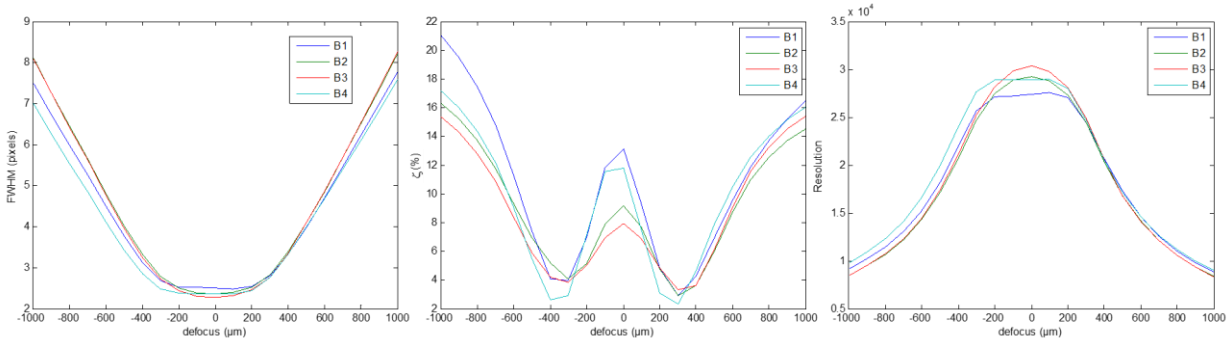

(a) (b) (c)

Figure 12. Sensitivity of the (a) FWHM, (b) likeness to a gaussian function and (c) resolution for the minimum wavelength of each spectral band

We can note that at +200 µm of defocus, the resolution is still high (greater than 26000) and that we are close to a minimum in the ξ curve. In order to be sure that such a working point is adequate, we also compute the absolute value of the difference between the ISRF at the nominal focus position and an ISRF at a defocused plane, called ε. Indeed, we don't want the shape of the ISRF to evolve during the launch and the lifetime of the instrument, so it must remain as close as possible as the shape it will have during the performances tests under vacuum on ground. The curves are plotted in Figure 13.

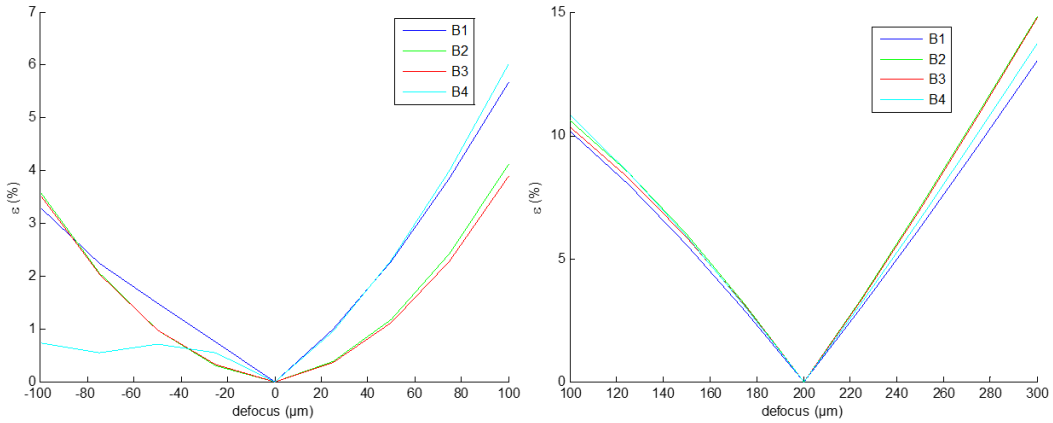

(a) (b)

Figure 13. Sensitivity of the evolution of the ISRF to the defocus, at two nominal working points: (a) focused position, and (b) +200 µm of defocus

The asymmetry of the curves, especially for B4, around the focused position is explained by the asymmetry of the ISRF, as seen in Figure 10.
We can see here that the working point at +200 µm of defocus is between two and three times more sensitive than the focused nominal working point. Given the instrumental risks implied by this sensitivity, we decided to not defocus the spectrometer. However, we keep on working on this question of potentially problematic non-uniform scenes, with the help of the analytical tool presented in this paper.

5. CONCLUSION

To conclude, we saw that the analytical model of the ISRF proposed by ADS has been carefully validated at CNES and ADS, with a numerical model with CODE V on one hand, and with experimental data on the other hand.
This model gives very accurate results, as it takes into account the diffraction effects that occur in the instrument, and whose impacts on the performances are important. As the WFE of the instrument is also considered, we are confident in the fact that this model provides us the theoretical performances of the MicroCarb instrument with a good reliability.
With it, we have been able to carry out technical trade-offs on some key elements of the instrument: the size of the grating and the slit, the adding of defocus or not.
Finally, we now own a fully validated model that allows us to evaluate the ISRF of any complex scene and use it at higher level to see the impact on the mission. This tool will also be useful to verify the results obtained during the on-ground performance tests of the instrument, by using as-built information of the components.

REFERENCES

[1] Rene Berlich, "Technical Note on FLORIS diffraction limitations", TEC-MMO/2013/63, iss 2, date 21/08/2013.
[2] Pasternak, F., Bernard, P., Georges, L. and Pascal, V., "The MicroCarb instrument", Proc. SPIE 10562, International Conference on Space Optics — ICSO 2016, 105621P (25 September 2017).
[3] CODE V Generalized Beam Propagation and Coupling Efficiency Reference Manual: Chapter 3 Beam Synthesis Propagation (BSP).